Journal of Physics:
Condensed Matter

PAPER • **OPEN ACCESS**

Ferrimagnetism and half-metallicity in Cr-substituted $Mn_{4-x}Cr_xAl_{11}$

To cite this article: M F B Noor *et al* 2025 *J. Phys.: Condens. Matter* **37** 235704

OPEN ACCESS
IOP Publishing
Journal of Physics: Condensed Matter
J. Phys.: Condens. Matter **37** (2025) 235704 (11pp)
https://doi.org/10.1088/1361-648X/add8d8

Ferrimagnetism and half-metallicity in Cr-substituted $Mn_{4-x}Cr_xAl_{11}$

M F B Noor[1], K-M Law[2], N Yasmin[1], A J Hauser[2] and T Besara[1,*]

[1] Department of Physics, Astronomy, and Materials Science, Missouri State University, Springfield, MO 65897, United States of America
[2] Department of Physics and Astronomy, University of Alabama, Tuscaloosa, AL 35487, United States of America

E-mail: tigletbesara@missouristate.edu

Received 25 February 2025, revised 1 May 2025
Accepted for publication 13 May 2025
Published 22 May 2025

Abstract

Single crystals of disordered $Mn_{4-x}Cr_xAl_{11}$ have been synthesized via the flux method. EDS on several crystals of various sizes and shapes revealed an average molar ratio of 17:9:74 for Mn:Cr:Al, while x-ray diffraction on three different crystals yield compositions $Mn_{2.26}Cr_{1.74}Al_{11}$ ($Mn_{4-x}Cr_xAl_{11}$, $x = 1.74$), $Mn_{0.83}Cr_{3.17}Al_{11}$, and $Mn_{1.07}Cr_{2.93}Al_{11}$. This compound crystallizes in space group $P\bar{1}$, isostructural with both Mn_4Al_{11} and Cr_4Al_{11}. Magnetic measurements on several crystals show that this disordered compound is ferrimagnetic with a low effective moment of μ_{eff} $1.012 \sim 0.004\mu_B$/f.u. and a non-reachable transition temperature. Density functional theory calculations display opening of a bandgap in the spin-up channel near the Fermi level with increasing Cr content, an indication of half-metallicity.

Keywords: ferrimagnetism, half-metallicity, disordered structure, single crystal growth, flux synthesis

1. Introduction

The Al–Mn phase space is rich in compounds, especially on the Al-rich side [1], and several comprehensive studies have been devoted to it [2–6]. Alloys and compounds in this phase space have been studied for a variety of properties, e.g. in electrical applications [7], as permanent magnets [8, 9], for solidification under pulsed magnetic fields [10], hardness and corrosion [11], decomposition behavior [12], cooling rate on microstructures [13], and for their effect on Mg–Al alloys [14–17], to name a few. The discovery of the first quasicrystals was also within this phase space ($Al_{86}Mn_{14}$) [18], giving rise to a new area of research [19]. Furthermore, half-metallicity was first predicted in Mn-containing Heusler alloys [20] and have since then been predicted and explored experimentally in more systems containing Al and Mn [21–34] of which some also contain Cr in addition to the two aforementioned elements [32, 35].

Within the Al–Mn phase space, the structure of Mn_4Al_{11} (δ-MnAl) was first determined by Bland in 1958 [36], suggesting a triclinic or pseudo-monoclinic structure. The structure was later confirmed by Kontio *et al* [37] and was shown to be a low-temperature phase of Mn_4Al_{11}. The high-temperature phase crystallizes in an orthorhombic structure [2, 38]. The magnetism of the low-temperature phase was explored by Dunlop and Grüner [39] where they observed a smooth cusp in both susceptibility and resistivity at approximately 100 K, a sign of a one-dimensional behavior. They attributed this to the crystal structure and to the absence of long-range interactions due to the strong interaction between a Mn atom and its nearby Al atoms suppressing interactions between Mn moments. They concluded that the magnetic properties are mainly determined

* Author to whom any correspondence should be addressed.

by the independent Mn-chains while the resistivity properties are determined by scattering of conduction electrons [39].

Compounds isostructural to triclinic Mn_4Al_{11} were also discovered later, Re_4Al_{11} [40] and Cr_4Al_{11} [41], although no magnetization studies has been performed on them. In addition, the ternary Al–Cr–Mn phase space was explored by Grushko *et al* [42]. They discovered compositions along the Al_3Cr–$Al_{11}Mn_4$ line, thus confirming a range of compositions isostructural to the triclinic $Al_{11}(Mn,Cr)_4$ phase.

In this study we report on the single crystalline growth, structure, and magnetization of disordered compounds within the $Mn_{4-x}Cr_xAl_{11}$ phase. Specifically, detailed single crystal x-ray diffraction on one crystal shows composition $Mn_{2.26}Cr_{1.74}Al_{11}$ ($Mn_{4-x}Cr_xAl_{11}$, $x = 1.74$), which is isostructural with T_4Al_{11} (T = Mn, Cr, Re). In addition, we show that this disordered compound exhibits ferrimagnetism, unlike the one-dimensional magnetic behavior observed in Mn_4Al_{11} [39]. Finally, we shed light on the magnetic character of this compound via density functional theory (DFT) calculations and show that it may exhibit half-metallicity.

2. Methods

Synthesis. We grew single crystals of $Mn_{4-x}Cr_xAl_{11}$ via the self-flux method with aluminum acting as the flux element. We measured and loaded 2 mmol of Mn, 1 mmol of Cr, and 20 mmol of Al, all 99.9%+, in a 2 ml alumina crucible. The Mn:Cr ratio was chosen as 2:1 since the original goal was an attempt to synthesize single crystals of the Heusler alloy Mn_2CrAl with Al as a self-flux. A second alumina crucible was filled with quartz wool and placed upside-down on top of the crucible holding the chemicals. In order to keep the reaction in an inert condition, we inserted the crucible ensemble in a quartz ampoule and capped the open end of the ampoule with parafilm, inside an argon-filled glovebox. The quartz ampoule was then pulled out of the glovebox, the parafilm was removed and the ampoule was quickly attached to a Schlenk line and sealed under vacuum using an oxygen-hydrogen torch. The ampoule was subsequently heated to 1000 °C at a rate of 50 °C h^{-1} in a programmable muffle furnace, maintained at this temperature for 15 h to allow the elements to soak well in the Al flux, and then slowly cooled to 750 °C at a rate of 2.5 °C h^{-1}, about 90 °C above the flux solidification/melting point. After reaching this temperature, the ampoule was rapidly taken out of the furnace, flipped upside-down, and immediately centrifuged to separate the crystals from the molten flux. The quartz wool inside the crucible cap acted as a filter to allow the liquid aluminum to pass through but restrict the solid crystals from passing through. The ampoule was then broken, and crystals were harvested at ambient temperature. The crystals are stable in the air.

Energy dispersive spectroscopy (EDS). We performed EDS employing a FEI QUANTA 200 FEG scanning electron microscope equipped with an Oxford Instruments Ultim Max EDS detector. We performed measurements at 20 kV on several crystals of various sizes and shapes to verify the proper stoichiometric ratios of the compound. All crystals were mounted on copper tape with a flat surface facing up.

X-ray diffraction. We performed single-crystal x-ray diffraction employing a Rigaku-Oxford Diffraction XtaLAB Synergy-S diffractometer equipped with a HyPix-6000HE Hybrid Photon Counting detector and dual PhotonJet-S Mo/Cu 50 W Microfocus x-ray sources. We collected reflections at room temperature with Mo Kα radiation ($\lambda = 0.71073$ Å) using ω scans with 0.5° frame widths to a resolution of approximately 0.4 Å, equivalent to 2θ 125°, and they were recorded, indexed, and corrected for absorption using Rigaku Oxford Diffraction CrysAlisPro [43]. We refined the structure with CRYSTALS [44] employing the charge-flipping software SUPERFLIP [45] to solve the structure. The quality of the data allowed for an unconstrained full matrix refinement against F^2 with anisotropic displacement parameters for all atoms. A CIF for the composition $Mn_{2.26}Cr_{1.74}Al_{11}$ ($Mn_{4-x}Cr_xAl_{11}$, $x = 1.74$) has been deposited with the Cambridge Crystallographic Data Center (CSD #2272254) [46].

Magnetization. The magnetic measurements were performed at the Cornell Center for Materials Research, where they employed a Quantum Design MPMS-3 system. They obtained zero field-cooled magnetization as a function of temperature at an applied field of 0.1 T while sweeping the temperature at a rate of approximately 0.1 K s^{-1}, and magnetization as a function of field at temperatures 2.0 K and 300 K while sweeping the field at a rate of approximately 50 Oe s^{-1} between 2 and 2 T and 100 Oe s^{-1} between 2 (–2) and 7 (–7) T. The sample comprised several, randomly aligned single crystals totaling a mass of approximately 14.6 mg.

DFT. Density functional theory calculations were performed using the Quantum Espresso 6.8 package. Spin-polarized self-consistent calculations were done using the projector augmented wave method in the scheme of generalized gradient approximation. The scalar-relativistic Perdew–Burke–Ernzerhof pseudopotentials used are generated by A. Dal Corso and can be found on the Quantum Espresso ready-to-use PSlibrary [47]. An automatically-generated Monkhorst–Pack k-point grid of size $6 \pm 6 \pm 6$ and energetic convergence threshold of 10^{-9} Ry was used for calculating magnetic moment and cohesive energy. For the final self-consistent calculation preceding a density-of-states (DOS) calculation, a $10 \pm 10 \pm 10$ k-point grid was used instead and with the same energetic convergence threshold.

3. Result and discussion

3.1. Structure

The reaction produced a high yield of small (≈0.1–0.2 mm on each side) crystals of indefinite shapes. The original goal was to grow single crystals of the cubic Heusler alloy Mn_2CrAl,

however, the shape of the crystals hinted at a different compound. EDS confirmed that the elemental composition was not that of the expected Heusler alloy. EDS results taken on several crystals of various sizes and shapes revealed molar ratios of Mn:Cr:Al to be 17:9:74 on average, to within 1–3 atomic percent. Clearly, the ratios do not match that of Mn_2CrAl but rather indicate a (Mn + Cr):Al ratio of approximately 1:3 (≈25:75) of which Mn is about twice that of Cr for a final Mn:Cr:Al atomic ratio of approximately 2:1:9.

X-ray diffraction collected on single crystals showed that this compound crystallizes in a triclinic space group. A search in the Inorganic crystal structure database [48] revealed no matching ternary structures with the approximate molar ratios as given by EDS and with a triclinic structure. After a careful refinement of the x-ray diffraction data, it was clear that this compound is a mixed-site isostructure of the binary compounds Mn_4Al_{11} and Cr_4Al_{11} [4, 5, 36, 37, 41, 49]. X-ray diffraction was collected on three different crystals with varying final compositions. We report here the full diffraction data and structural analysis for one of them. This specific compound crystallizes in $P\bar{1}$ (#2) with lattice parameters $a = 5.11920(3)$ Å, $b = 8.91768(6)$ Å, $c = 5.06184(5)$ Å, $\alpha = 89.4217(7)°$, $\beta = 100.5735(7)°$, and $\gamma = 105.6830(6)°$. See table 1 for a complete list of parameters and diffraction data.

Both transition metal sites in this compound are disordered, and in unequal amount: for this particular crystal, while site 1 (M1 = Mn11 and Cr12) has an Mn site occupancy factor (SOF) of 0.64(2) and a Cr SOF of 0.36(2), site 2 (M2 = Mn21 and Cr22) has an approximately equal split: 0.49(2):0.51(2) for Mn:Cr. The SOFs of the six Al sites were also relaxed in subsequent refinements but displayed negligible deviations from full occupancy. Close attention was paid to the Al6 atom which was reported as approximately half-occupied by Kontio *et al* [37] in Mn_4Al_{11}. We, however, do not observe this and nor was it observed in Cr_4Al_{11} [41] and Re_4Al_{11} [40]. The SOFs for all Al sites were therefore fixed to full occupancy in the final refinement. Additionally, trying to fix either of the transition metal sites to fully occupied Mn or Cr while relaxing the SOF of the other site resulted in worse refinement residuals and with atomic ratios that deviated too much from the EDS results. We therefore conclude that both transition metal sites are mixed. We also tried Al mixing into the metal sites, but this resulted in negative Al SOFs. The final stoichiometry was refined to $Mn_{2.26}Cr_{1.74}Al_{11}$ ($Mn_{4-x}Cr_xAl_{11}$, $x = 1.74$), yielding the approximate molar ratios 15.1:11.6:73.3 for Mn:Cr:Al, not quite matching the averaged EDS result but is within a few atomic percent. Table 2 lists the final SOFs and the atomic coordinates for this crystal. The final stoichiometries on the two other crystals refined to $Mn_{0.83}Cr_{3.17}Al_{11}$ and $Mn_{1.07}Cr_{2.93}Al_{11}$. The transition sites in the $x = 3.17$ crystal have Mn:Cr ratios of 0.34:0.66 for site 1 and 0.08:0.92 for site 2, while in the $x = 2.93$ crystal, the ratios are 0.41:0.59 for site 1 and 0.13:0:87 for site 2.

Figure 1 shows the unit cell with the two transition metal sites colored according to the mixing ratios of $Mn_{2.26}Cr_{1.74}Al_{11}$: M1 with 0.64 Mn (magenta) and 0.36 Cr (blue) and M2 with 0.49 Mn and 0.51 Cr. Figure 2 shows the local Al environment around M1 and M2. Each metal site is ten-coordinated by Al atoms in a non-obvious symmetry but was described as bicapped distorted cubic arrangement for the binary Mn_4Al_{11} [37]. M1 is surrounded by Al of all six different crystallographic sites (three Al1, three Al2, one Al3, one Al4, one Al5, and one Al6) while *M*2 is surrounded by five of them (one Al1, one Al2, three Al3, three Al4, and two Al5).

Table 1. Single crystal x-ray diffraction data and parameters for $Mn_{2.26}Cr_{1.74}Al_{11}$, collected at room temperature.

Parameters	$Mn_{4-x}Cr_xAl_{11}$ ($x = 1.74$)
Stoichiometry	$Mn_{2.26}Cr_{1.74}Al_{11}$
Molecular weight (g mol^{-1})	511.41
Space group	$P\bar{1}$ (#2)
a (Å)	5.11920(3)
b (Å)	8.91768(6)
c (Å)	5.06184(5)
α (°)	89.4217(7)
β (°)	100.5735(7)
γ (°)	105.6830(6)
V (Å^3)	218.509(3)
Z	1
ρ_{calc} (g cm^{-3})	3.886
Absorption coefficient μ (mm^{-1})	6.330
Absorption corrections T_{min}, T_{max}	0.33, 0.58
Crystal size (mm^3)	0.086 × 0.137 × 0.146
Data collection range (°)	$2.374 < \theta < 68.887$
h range	$-13 \leqslant h \leqslant 13$
k range	$-23 \leqslant k \leqslant 23$
l range	$-13 \leqslant l \leqslant 10$
Reflections collected	69 404
Independent reflections	8154
Parameters refined	57
$\Delta\rho_{min}$, $\Delta\rho_{max}$ (e Å^{-3})	–0.99, 1.25
R_{int}	0.024
$R_1(F)$ for all data[a]	0.0172
$wR_2(F_O^2)$[b]	0.0535
Goodness-of-fit on F^2	1.0000
CSD #	2272254

[a] $R_1 = \Sigma||F_O|-|F_C||/\ \Sigma|F_O|$.
[b] $wR_2 = [\Sigma w(F_O^2\ \ F_C^2)^2/\Sigma w(F_O^2)^2]^{1/2}$, $w = 1/[\sigma^2(F_O^2) + (A\ P)^2 + B\ P]$, $P = [2F_C^2 + \mathrm{Max}(F_O^2,0)]/3$ where $A = 0.01$ and $B = 0.23$.

As has been mentioned, the discovered compound of $Mn_{2.26}Cr_{1.74}Al_{11}$ is not a unique stoichiometry in this Mn_4Al_{11} isostructure: a range of compositions have been mapped out in the Al–Cr–Mn ternary phase diagrams and this particular phase appears in the 800 °C and 900 °C ternary phase diagrams, labeled as the ν-phase, or $Al_{11}Mn_4$(LT) [42, 50]. The 800 °C phase diagram has been reproduced from [50] in figure 3, showing that the ν-phase ranges from 100% Mn in the transition metal site (Mn_4Al_{11}) to approximately $Mn_3Cr_{22}Al_{75}$ ($Mn_{0.12}Cr_{0.88}Al_3$). As has been shown by x-ray diffraction refinements on two other crystals, we have formed a range of compositions within this ν-phase range. The composition $Mn_{2.26}Cr_{1.74}Al_{11}$ has been marked with a red dot in the ternary phase diagram in figure 3.

Table 2. Atomic coordinates, and equivalent displacement parameters of $Mn_{2.26}Cr_{1.74}Al_{11}$.

Atom	SOF	Site	x	y	z	U_{eq} (Å^2)
M1	0.64(2) Mn + 0.36(2) Cr	2*i*	0.39103(1)	0.13371(1)	0.33691(1)	0.0052(1)
M2	0.49(2) Mn + 0.51(2) Cr	2*i*	0.85724(1)	0.40322(1)	0.70032(1)	0.0074(1)
Al1	1	2*i*	0.53337(5)	0.12502(3)	0.84648(5)	0.0082(1)
Al2	1	2*i*	0.89627(5)	0.12517(3)	0.48745(5)	0.0084(1)
Al3	1	2*i*	0.33311(5)	0.37307(3)	0.57533(5)	0.0082(1)
Al4	1	2*i*	0.71916(5)	0.36904(3)	0.18271(5)	0.0095(1)
Al5	1	2*i*	0.16997(5)	0.31883(3)	0.05623(5)	0.0109(1)
Al6	1	1*a*	0	0	0	0.0100(1)

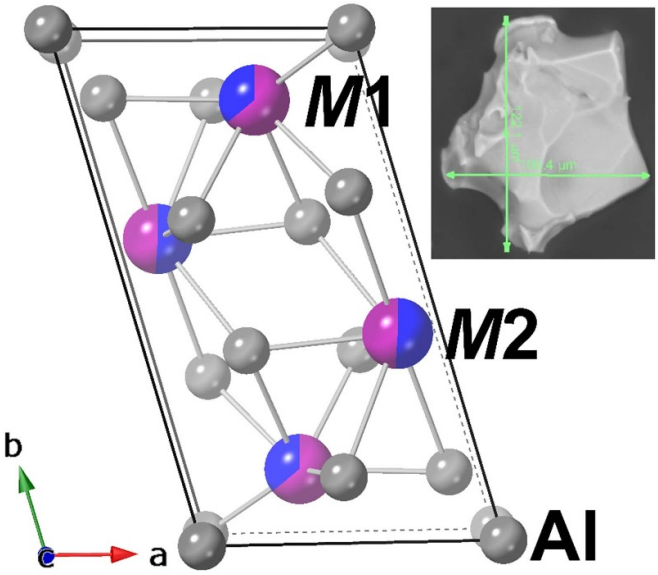

Figure 1. Unit cell of $Mn_{2.26}Cr_{1.74}Al_{11}$ viewed along the *c*-axis. The mixed metal sites are colored blue and magenta and display the mixing ratios where Mn is represented by the magenta and Cr by the blue color. M1 comprises 0.64(2) Mn and 0.36(2) Cr while M2 comprises 0.49(2) Mn and 0.51(2) Cr. The Al atoms are colored gray. The inset shows a single crystal of no particular shape, which was typical for this compound.

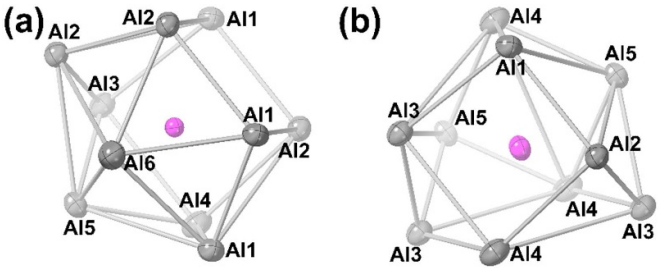

Figure 2. Local atomic environment around (a) M1 and (b) M2 viewed along the (111) axis. Each metal site is surrounded by ten Al atoms. The anisotropic displacement ellipsoids are drawn at the 95% probability level.

3.2. Magnetism

The magnetism of the binary Mn_4Al_{11} has been explored previously [39] but—as far as we can tell—no magnetic study has been performed on the Cr_4Al_{11} and Re_4Al_{11} binaries, nor

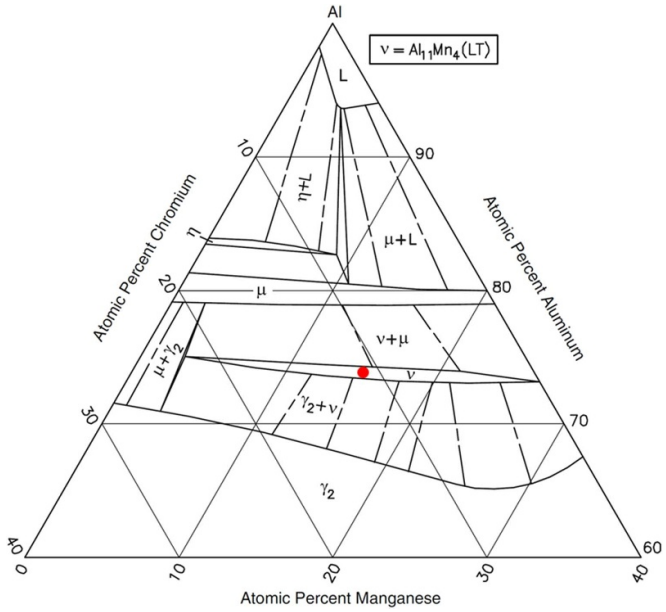

Figure 3. Ternary Al–Cr–Mn phase diagram at 800 °C in the Al-rich region. Adapted from [50], with permission from Springer Nature.

on any sample in the $(Mn,Cr)_4Al_{11}$ phase range described in [42, 50]. It was shown that Mn_4Al_{11} has a one-dimensional magnetic character evidenced by a smooth cusp at around 100 K in both magnetic susceptibility and electric resistivity [39]. In addition, the authors reported no long-range magnetic order below that temperature based on neutron diffraction collected at 4.2 K. A plausible explanation for the one-dimensional character was given based on the crystal structure in which the Mn atoms arrange themselves roughly in …*AABBAABB*… chains where *A* and *B* are the two metal sites and with distances 3.188 Å, 3.198 Å, and 3.053 Å for *AA*, *AB*, and *BB*, respectively.

Figure 4(a) displays our structure again but without the Al-atoms to highlight the transition metals and the distances between them. The view is along the *a*-axis and in perspective mode. We have an M1–M1 distance of 3.216 Å (alternating gray and green and equivalent to the *AA* distance in [39]), an M2–M2 distance of 2.980 Å (alternating gray and red and equivalent to the *BB* distance), and an M1–M2 distance of 3.199 Å (solid gray and equivalent to the *AB* distance). These three distances define the chains while the

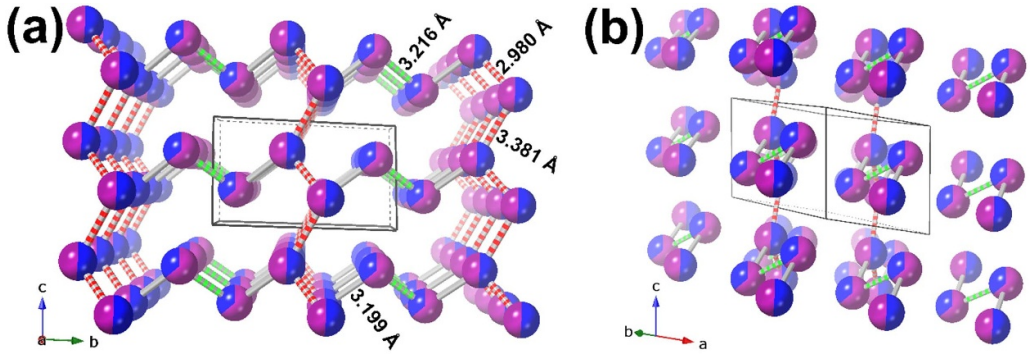

Figure 4. (a) View in perspective mode along the *a*-axis of the $Mn_{2.26}Cr_{1.74}Al_{11}$ structure but without the Al atoms. The atom colors are as in figure 1. The alternating gray and green 'bond' defines the M1–M1 distance of 3.216 Å, the alternating gray and red bonds define the M2–M2 distances of 2.980 Å and 3.381 Å (roughly along the *c*-axis), and the solid gray defines the M1–M2 distance of 3.199 Å. (b) View along (110).

M2–M2 distance of 3.381 Å (also alternating gray and red) links the chains together along the (113) direction. The chains are along the (110) axis as can be viewed in figure 4(b) (into the page). While it is clear what Dunlop and Grüner [39] meant by one-dimensional chains, in our structure the interchain M2–M2 distance 3.381 Å is not very much longer than the intrachain distances, plausibly resulting in a two-dimensional arrangement of metal sites instead. The next shortest interchain distance is approximately 4.63 Å. An argument for one-dimensional character could be regarding the locations of the Al atoms (not shown in figure 4). Al5 and Al6 atoms separate the chains from each other in the [001] plane while Al3 atoms separate the chains from each other in the $[1\bar{1}0]$ plane; the other Al atoms are located roughly within the chains. The presence of the Al5 and Al6 atoms in the plane separating the chains could be why Dunlop and Grüner declared the presence of one-dimensional chains. They did not specify the nature of the ordered state, whether the coupling between neighboring Mn-atoms along the chain was of ferro-, antiferro-, or ferrimagnetic nature; however, one can surmise from their susceptibility plot (figure 1 in [39]) that the interaction seems to be of antiferromagnetic nature.

We performed magnetic measurements on our mixed-site sample comprising several randomly oriented crystals of varying composition as discussed above in connection with the ternary phase diagram. Figure 5 displays the magnetization as a function of temperature from 2 K to 300 K, obtained at an applied field of 0.1 T. The curve looks paramagnetic or possibly ferromagnetic down to the lowest temperature [51], and we observed no smooth cusp and therefore no evidence for a low-dimensional character. It is possible that the Mn/Cr mixing at the two metal sites in $Mn_{4-x}Cr_xAl_{11}$ and the mix of crystals with different Mn:Cr disorder removed or smeared out the low-dimensional magnetic character, especially since Mn and Cr couple differently to each other (parallel vs. antiparallel). The situation is also more complex since the two sites are mixed in unequal amounts and differ from crystal to crystal.

Looking at the inverse susceptibility as a function of temperature (figure 5 inset), however, reveals a hyperbolic curve, a signature of ferrimagnetism [52–55]. Ferrimagnetism in this

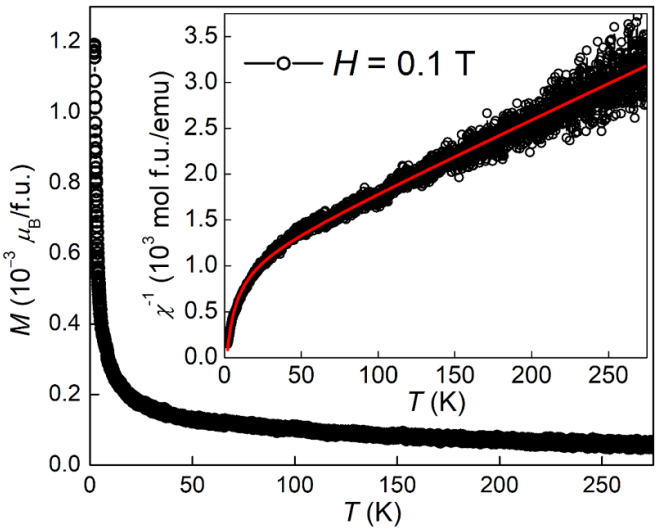

Figure 5. Magnetization as a function of temperature at an applied field of 0.1 T. Inset: Inverse susceptibility as a function of temperature. The hyperbolic trend is a sign of ferrimagnetism. The red line is a fit to equation (1).

material is plausible with the two different metal sites comprising different mixings of Mn and Cr. The addition of Cr into a Mn site will change the magnetic moment of that site so that—if the two sites originally had equal and antiparallel magnetic moments—the moments now become unequal.

Assuming two sublattices for simplicity (the situation is of course more complex with different mixings at the two sites and with a sample comprising crystals of varying compositions), the inverse susceptibility can be expressed with the molecular field theory as [52–55]

$$\frac{1}{\chi} = \frac{T \quad \theta}{C} \quad \frac{\zeta}{T \quad \theta'}, \tag{1}$$

where C is the Curie constant and related to the effective moment μ_{eff} via $C = N_A\mu_B^2\mu_{\text{eff}}^2/3k_B$, θ is the Curie–Weiss temperature, and ζ and θ' are parameters containing information about the magnetization of the two sublattices. The parameter

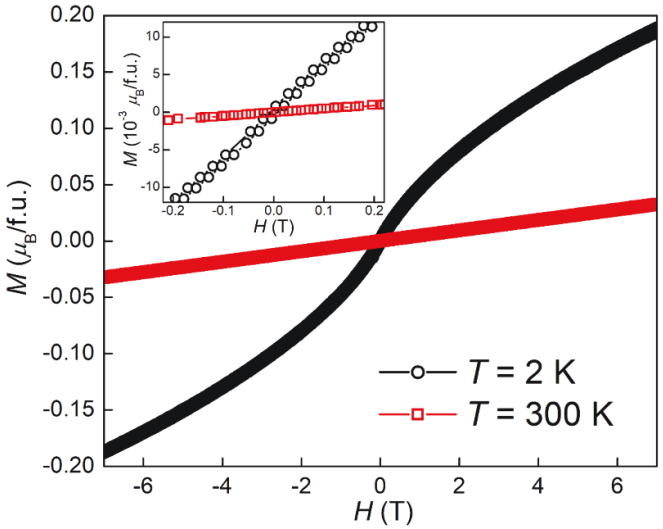

Figure 6. Magnetization as a function of applied field at 2 K (black circles) and 300 K (red squares). The inset focuses on the low-field region showing essentially zero hysteresis.

θ' defines the hyperbola asymptote and should therefore have a lower value than an actual transition temperature (see figure 3 in [53]). The experimental data fits quite well to equation (1) and is shown as a solid red line in the inset to figure 5. The fitting parameters are μ_{eff} $1.012 \sim 0.004$ μ_B/f.u., θ $136 \sim 3$ K, ζ $6641 \sim 548$K $\times$mol emu^{-1} and θ' $4.7 \sim 0.7$ K. The low effective moment is an indication of site-mixing and ferrimagnetism in this compound. Furthermore, $\theta < 0$ and $\zeta > 0$ point towards ferrimagnetic ordering below the transition temperature ($\theta < 0$ and $\zeta = 0$ for antiferromagnetism and $\theta > 0$ and $\zeta = 0$ for ferromagnetism). Since the magnetic measurements were performed on a sample containing several randomly oriented crystals of varying composition (as discussed above), the two-sublattices approximation is the best that can be done. To include the different site-mixings in the model would require magnetization measurements to be performed on a single crystal, which is not feasible due to the small size (low mass) of the crystals, or on multiple crystals all confirmed to have the exact same stoichiometry.

Figure 6 displays the magnetization as a function of applied field at 2 K and 300 K. In both cases, saturation is not reached, and essentially no hysteresis is observed (inset). The non-saturation and linearity of isotherms have been observed in other ferrimagnets, such as the half-metallic fully compensated ferrimagnets (CrFe)S [56] and $Mn_{1.5}FeV_{0.5}Al$ [57], and the Co–Mn–V–Al [23] and $(CoCrFeNi)_{1-x}Mn_x$ [58] alloys. This non-saturation is a typical behavior of the paramagnetic region, confirming that we have not yet reached the transition temperature to the ferrimagnetic state.

3.3. DFT

DFT calculations are by definition performed for a material system at zero kelvin, i.e. thermodynamics is ignored in the Kohn–Sham equations. As such, even though our magnetization measurements have not reached past the transition temperature, we may still expect ferrimagnetism to result from DFT calculations of a reasonably accurate crystallographic model of our sample. In order to corroborate our experimental results, we performed DFT calculations on a set of theoretical samples with increasing Cr content starting from pure Mn to pure Cr: Mn_4Al_{11}, Mn_3CrAl_{11}, $Mn_2Cr_2Al_{11}$, $MnCr_3Al_{11}$, and Cr_4Al_{11}. The results are summarized in table 3. Due to computational power limitations, the calculations were performed on a single unit cell; therefore, Mn and Cr substitutional and antisite disorders at the M1 and M2 lattice sites have not been considered. For these single-unit-cell crystal structures, inversion symmetries about the center of the unit cell ($(1/2,1/2,1/2)$ in crystal coordinates) allow for atomic swapping between certain pairs of M sites with no changes to calculation results. Therefore, in terms of the replacement of Mn by Cr atoms, there are two distinct configurations that contain one Cr, three configurations that contain two Cr, and two configurations that contain three Cr. Furthermore, each configuration may support more than one magnetic ground state: the M1 site magnetic moments can be parallel or antiparallel, and likewise for the M2 site moments; this further leads to four possible magnetic states for each of the configurations listed. To exhaust the list of possible magnetic states for each atomic configuration, multiple calculations with different starting atomic magnetizations are performed where appropriate. We opted not to report the formation energy of our results; instead, as is the convention in the literature, we will only be comparing the cohesive energies between configurations that have the same molecular formula. The magnetic ground state for any given configuration is thus the one with the lowest cohesive energy.

We observed that a general statement can be made based on the atomic moments and cohesive energies of converged calculations: for those configurations i.e. placement of Mn and Cr atoms on the two M1 and M2 sites, in which the resulting structure respects the inversion symmetry of the base Mn_4Al_{11} structure(these configurations are where exactly one atomic species occupy two M1 sites or two M2 sites as in Mn–Mn–Mn–Mn, Mn–Mn–Cr–Cr, Cr–Cr–Mn-Mn, and Cr–Cr–Cr–Cr), their magnetic ground states are also ones that respect this symmetry. For instance, we found two magnetic states for the Mn–Mn–Cr–Cr configuration. In one, the M1 sites are identical in both atomic species and magnetic moment (Mn; 0.0283 μ_B); likewise, for the M2 sites (Cr; 1.4655 μ_B). On the other hand, in another calculated convergent magnetic state for this configuration, each of the four M sites instead have a different magnetic moment—therefore, this magnetic state does not possess the inversion symmetry as does the atomic lattice. We observed that calculations for the latter magnetic state yielded a higher cohesive energy, i.e. less thermodynamically stable. The above would suggest that, for the magnetic ground states of this material system (which includes all atomic configurations), the magnetic moment of any one M-site atom couples strongly to the moments of its (nearest-)neighboring M-site atoms, that the symmetries of the atomic lattice becomes important to the magnetic properties of the compound. Naturally, those (nearest-)neighboring M-site atoms should also include the M-site atoms of the adjacent unit cells; thus, the need for a supercell—to establish a complete

Table 3. Magnetic moment results from DFT calculations on a single unit cell with different atomic configurations of Mn and Cr. The configuration order refers to the metal sites M1–M1–M2–M2. Multiple entries of the same configuration are convergent magnetic states; those which have the lowest cohesive energies of their respective configuration are bolded. Italic numbers indicate negative atomic magnetic moments while regular numbers indicate positive atomic magnetic moments. Positive moment is along the positive direction of the crystal *c*-axis.

			M-site magnetic moment (μ_B)				
Atoms	Configuration M1–M1–M2–M2	Cohesive energy (Ry)	Atom 1	Atom 2	Atom 3	Atom 4	Total moment (μ_B/cell)
4 Mn	Mn–Mn–Mn–Mn	**−1580.913 624**	***−0.4298***	***−0.4298***	**1.4170**	**1.4170**	**1.75**
		−1580.901 632	−0.196	0.1961	0.9875	*−0.9875*	0.00
3 Mn + 1 Cr	Mn–Mn–Cr–Mn	**−1542.585 911**	***−0.1629***	***−0.4518***	**1.1969**	**1.4962**	**2.01**
	Cr–Mn–Mn–Mn	−1542.577 125	*−0.1749*	*−0.5472*	1.5891	1.4614	2.08
2 Mn + 2 Cr	Cr–Cr–Mn–Mn	**−1504.236 578**	***−0.526***	***−0.5261***	**1.7456**	**1.7454**	**2.08**
		−1504.219 578	0.2814	0.4482	*−1.4916*	1.3787	0.62
	Cr–Mn–Cr–Mn	**−1504.246 549**	**0.2608**	***−0.4175***	**1.5711**	**1.6197**	**3.00**
	Mn–Mn–Cr–Cr	**−1504.254 758**	***−0.0283***	***−0.0283***	**1.4655**	**1.4655**	**2.99**
		−1504.246 790	0.1096	*−0.1100*	0.6810	*−0.6797*	0.00
1 Mn + 3 Cr	Mn–Cr–Cr–Cr	**−1465.912 694**	***−0.0747***	**0.3136**	**1.492**	**1.5444**	**3.47**
	Cr–Cr–Mn–Cr	−1465.904 344	0.2801	0.4848	1.7504	1.555	3.99
4 Cr	Cr–Cr–Cr–Cr	**−1427.568 214**	**0.5246**	**0.5246**	**1.4457**	**1.4457**	**4.11**

description of the magnetic ordering in this material system—becomes apparent.

In addition, we noticed a disagreement between our prediction of a ferrimagnetic ground state in Mn_4Al_{11} and the results reported by Dunlop and Grüner [39], which resembled one-dimensional spin chain with antiferromagnetic coupling. The reason behind this conflict is quite possibly that, again, our DFT calculation is performed over a single unit cell, which would not have captured for instance the antiferromagnetic chains suggested by Dunlop and Grüner. In fact, that single-unit-cell calculation yielded a ferrimagnetic ground state while antiferromagnetism was experimentally observed in [39], may even suggest an alternative explanation in which Mn_4Al_{11} is actually a fully-compensated ferrimagnet. Mn-containing fully-compensated ferrimagnets are not unheard of: their characteristic ultralow coercive field at the compensation temperature [59] has been observed [23, 26, 57].

Additionally, all our calculated total moments are larger than the experimentally obtained effective moment μ_{eff} $1.012 \sim 0.004\ \mu_B$ of our $Mn_{4-x}Cr_xAl_{11}$ samples, save for a total of three magnetic non-ground state for the configurations Mn–Mn–Mn–Mn, Mn–Mn–Cr–Cr, and Cr–Cr–Mn–Mn. It should be emphasized that the effective moment was obtained by fitting the inverse susceptibility to equation (1). The calculation for a $Mn_{4-x}Cr_xAl_{11}$ compound (with varying x), in which site-mixing is necessary, will likely result in a lower total moment that is more agreeable with the experimental result.

We would also like to point out that the range of cohesive energies across different atomic configurations (of the same Mn:Cr ratio) is exceedingly small. The largest cohesive energy difference of 0.04 Ry is between two specific magnetic states of different atomic configurations of 2 Mn + 2 Cr; however, within the other four Mn:Cr ratios, the difference between lowest and highest cohesive energy differences are no more than 0.01(2) Ry. Since for a given Mn:Cr ratio the various atomic configurations can be interpreted as site-swaps of each other, dividing those cohesive energy differences by the Boltzmann constant provides us with an estimate for the temperature regime in which M-site antisite disorder are relevant. This number ranges from 0.03–0.06 eV per M site per unit cell, which translates to 0–2 orders of magnitude lower than the ampoule temperature (in Celsius). This implies that any atomic configurations of a given Mn:Cr ratio are likely equally accessible during the formation of the sample. One can see this as a sign that site-mixing is a necessary factor to consider for an accurate description of this compound. Another (simpler) justification for performing future DFT calculations with site-mixing is as follows: since XRD shows that the M site of our samples are sufficiently disordered, we do not know of the concentration of unit cells with a particular Mn:Cr in a particular atomic configuration. Therefore, shall we want to average the calculation results of different atomic configurations and Mn:Cr ratios to simulate the results of a realistic sample (if one can even considered this a sound approach to employ), we will have to face the issue that we would not know the appropriate statistical weights for averaging.

We will now return to the discussions regarding magnetic moments of our DFT results. Due to the prevalence of integer moments in our calculated magnetic states, we suspect high

spin-polarization character in these compounds, on the basis of the generalized Slater–Pauling rule. Even though we have stressed the importance of M-site-mixing to the accuracy of calculated results, there is still knowledge to be gained from exploring the electronic behavior of these 'base' single unit-cell magnetic states. This is because we have performed preliminary DOS calculations for the magnetic ground states of the two stoichiometric endpoints, Mn_4Al_{11} and Cr_4Al_{11}; the two compounds exhibit striking similarities in broad DOS features and a spin-up bandgap (both compounds are metallic in the spin-down channel). Based on this observation, we posit that a spin-up bandgap appears in each other fractional Mn:Cr ratios (2:2, 3:1, etc) as well.

To explore this possibility, we selected the magnetic ground states for each possible Mn:Cr (1 Cr to all Cr) for DOS calculations. The spin-polarized DOS, plotted in figures 7(a)–(d) respectively, confirmed our suspicion (the spin-up gap shaded in grey): Mn–Mn–Mn–Mn (no Cr), Mn–Mn–Cr–Mn (1 Cr; magnetic ground state), Mn–Mn–Cr–Cr (2 Cr; magnetic ground state), and Cr–Cr–Cr–Cr (4 Cr). Of note, '3 Cr' is not shown, as we did not observe meaningful differences between the DOS for the magnetic ground states of '3 Cr' and '4 Cr', especially regarding the position and width of the spin-up gap.

We observed two phenomena that seemed to correlate with the addition of Cr atoms: (1) a general energy shift of DOS features towards higher energies, and (2) the gradual widening of a bandgap in the spin-up channel near the Fermi level. The energy shift of DOS features can be explained as a shift in the Fermi level towards lower energy due to a decrease in total number of valence electrons per molecular formula.

Regarding the bandgap, while a thorough understanding of its emergence with the introduction of Cr requires band structure calculations and likely some form of a molecular orbital hybridization model, we can nevertheless acquire some basic information simply from atom-specific projected DOS (PDOS) data (figure 8).

Near the Fermi level (∼2 eV), the M-site PDOS are dominated by *d*-orbital states regardless of atomic configurations (figures 8(a)–(f)); only a vanishing small number of states are associated to *s*- and *p*-orbitals (not shown). Similarly, Al PDOS are majorly *p*-orbital states (figures 8(g)–(j)). For each compound, one finds a high degree of similarity between the general shapes of M-site *d*-orbital and Al *p*-orbital PDOS: in both spin channels, a lobe below and above the Fermi level, joining near the Fermi level with the presence of a small spin-up gap. When comparing the total DOS (figure 7) and all atomic PDOS for each compound, one sees that both the lower and upper band edges of this spin-up gap consistently comprise a fair mixture of M-site and Al valence states. We understand this as a sign that extensive *p*–*d* hybridization is present between M-site (Mn and/or Cr) *d*-electrons and Al *p*-electrons. Thus, it is understandable that when one replaces a given Mn atom with a Cr atom within a unit cell, one would also alter the observed bandgap.

The presence of a gap in only one spin channel defines a half-metal. Half-metallicity entails fully spin-polarized

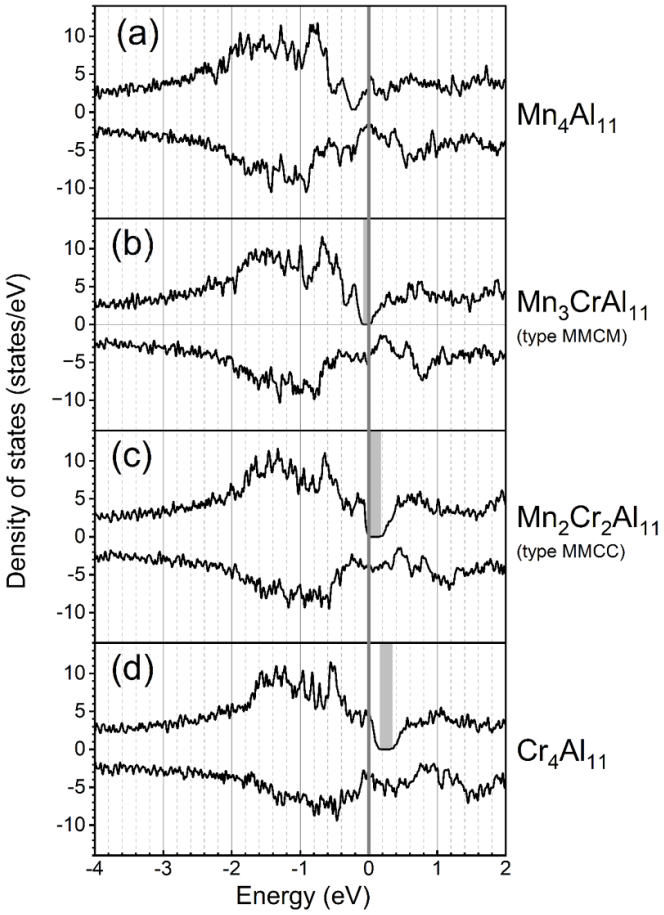

Figure 7. DOS for (a) Mn_4Al_{11}, (b) Mn_3CrAl_{11}, (c) $Mn_2Cr_2Al_{11}$, and (d) Cr_4Al_{11}. The solid gray line is the Fermi energy while the grey box is a guide-to-eye for the majority-band gap. In each figure, the upper (lower) curve represents the spin-up (spin-down) channel, where the positive *z*-direction is defined as the direction of the total magnetic moment. Zero energy is set at the Fermi level.

conductance, which has non-volatile memory applications. Half-metallicity was first predicted in Mn-containing Heusler alloys [20], and has been subsequently predicted in many more Mn-containing Heusler systems. On the other hand, the experimental observation of half-metallicity requires a more elaborated setup: the direct probing of a fully spin-polarized Fermi surface can be done by spin-polarized photoemission spectroscopy; less direct ways involve the observation of high magnetoresistance due to spin–orbit torque transfer in a half-metallic ferromagnet tunnel junction, or high spin-current generation in nonlocal measurements. It has been proposed that the resistivity of half-metals features a characteristic temperature scaling due to the inhibition of spin-flips [60]. This has been observed in at least one study, of the disordered Mn-containing Heusler alloy CoMnVAl [23]. Another Mn-containing alloy (not Heusler), Mn_3Al, has been calculated to feature half-metallicity [26, 28]; In [26], magnetic properties of Mn_3Al thin films were studied, though its half-metallicity were not characterized. Based on our DFT results, we can

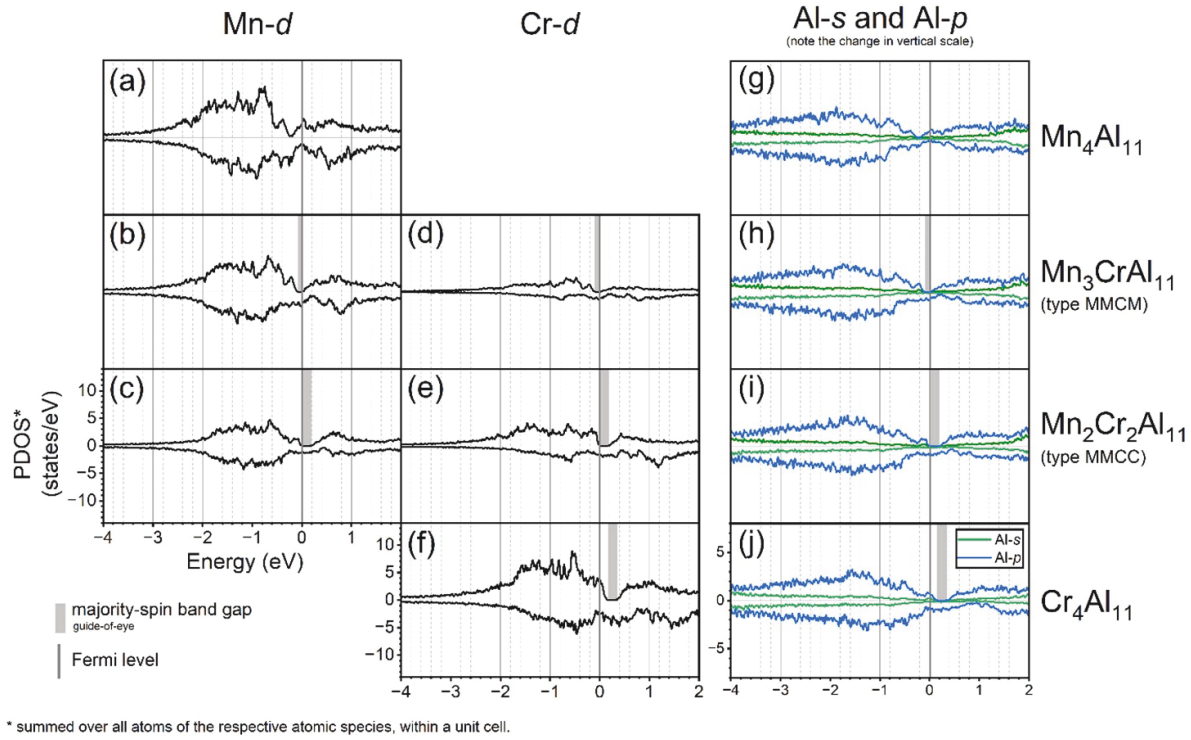

Figure 8. PDOS of the (a)–(c) Mn-*d* orbitals, (d)–(f) Cr-*d* orbitals, and (g)–(j) Al-*p* orbitals for Mn_4Al_{11}, Mn_3CrAl_{11}, $Mn_2Cr_2Al_{11}$, and Cr_4Al_{11}. The solid gray line is the Fermi energy while the grey box is a guide-to-eye for the majority-band gap.

surmise that our mixed $Mn_{2.26}Cr_{1.74}Al_{11}$ may be half-metallic at the temperature regime where it is a ferrimagnet; however, more in-depth DFT studies and thin film characterization are needed.

3.4. Conclusion

We have grown single crystals of $Mn_{4-x}Cr_xAl_{11}$, a mixed-sited version of the binaries Mn_4Al_{11} and Cr_4Al_{11} that crystallizes in the space group $P\bar{1}$. This specific phase exists in a range of compositions as can be seen in the Al–Cr–Mn ternary phase diagram and single crystal x-ray diffraction on one crystal yielded $Mn_{2.26}Cr_{1.74}Al_{11}$ ($Mn_{4-x}Cr_xAl_{11}$, $x = 1.74$) with lattice parameters $a = 5.11920(3)$ Å, $b = 8.91768(6)$ Å, $c = 5.06184(5)$ Å, $\alpha = 89.4217(7)°$, $\beta = 100.5735(7)°$, and $\gamma = 105.6830(6)°$. This structure has two transition metal sites and, in our compound, both are mixed: while one site has Mn:Cr SOF of 0.64:0.36, the other site has an approximately equal split, 0.49:0.51. Magnetic measurements reveal a ferrimagnetic compound, likely arising from the site-mixing with an effective moment of μ_{eff} $1.012 \sim 0.004$ μ_B/f.u.. This is in contrast to previous magnetic measurements on pure Mn_4Al_{11} which exhibited an antiferromagnetic transition. DFT calculations on a single unit cell of Mn_4Al_{11}, Mn_3CrAl_{11}, $Mn_2Cr_2Al_{11}$, $MnCr_3Al_{11}$, and Cr_4Al_{11}, show a ferrimagnetic ground state in Mn_4Al_{11}, Mn_3CrAl_{11}, and $Mn_2Cr_2Al_{11}$, and a ferromagnetic ground state in Cr_4Al_{11}. Further DOS calculations show an energy shift towards higher energies and the opening of a bandgap in the spin-up channel near the Fermi level, hinting at a possible half-metallic ferrimagnet. Further studies are underway in exploring a range of Mn-Cr mixings and their magnetic and electronic behavior.

Data availability statement

The data cannot be made publicly available upon publication because they are not available in a format that is sufficiently accessible or reusable by other researchers. The data that support the findings of this study are available upon reasonable request from the authors.

Acknowledgment

T.B. acknowledges the National Science Foundation (NSF) MRI program that funded the purchase of the Synergy-S X-ray diffractometer via award CHE-2117129. This work made use of a Quantum Design MPMS-3 supported by NSF (DMR-1920086) and the Cornell Center for Materials Research Shared Facilities which are supported through the NSF MRSEC program (DMR-1719875). T.B. also acknowledges financial support provided by Missouri State University's new faculty startup fund. K.M.L. and A.J.H. gratefully acknowledge financial support from NSF CAREER award DMR-2047251. A.J.H. also acknowledges financial support from the NSF under Grant DMR-2328830, supported in part by funds from federal agency and industry partners as specified in the Future of Semiconductors (FuSe) program.

ORCID iDs

K-M Law https://orcid.org/0000-0001-6392-2262
N Yasmin https://orcid.org/0009-0007-6824-203X
T Besara https://orcid.org/0000-0002-2143-2254

References

[1] Okamoto H, Schlesinger M E and Mueller E M (ed) 2016 Al (Aluminum) binary alloy phase diagrams *Alloy Phase Diagrams* (ASM International) pp 113–39
[2] Murray J L, McAlister A J, Schaefer R J, Bendersky L A, Biancaniello F S and Moffat D L 1987 Stable and metastable phase equilibria in the Al-Mn system *Metall. Trans. A* **18** 385–92
[3] Liu X J, Ohnuma I, Kainuma R and Ishida K 1999 Thermodynamic assessment of the aluminum-manganese (Al-Mn) binary phase diagram *J. Phase Equilib.* **20** 45–56
[4] Grushko B and Balanetskyy S 2008 A study of phase equilibria in the Al-rich part of the Al-Mn alloy system *Int. J. Mater. Res.* **99** 1319–23
[5] Wang J, Shang S-L, Wang Y, Mei Z-G, Liang Y-F, Du Y and Liu Z-K 2011 First-principles calculations of binary Al compounds: enthalpies of formation and elastic properties *Calphad* **35** 562–73
[6] Janotova I, Svec P Sr, Svec P, Matko I, Janikovic D and Mahalkovic M 2017 *Proc. 23 Int. Conf. on Applied Physics of Condensed Matter* (Slovak University of Technology) p 346
[7] Shen W, Hu A, Liu S and Hu H 2023 Al-Mn alloys for electrical applications: a review *J. Alloy. Metall. Syst.* **2** 100008
[8] Marenkin S F and Ril A I 2020 Al–Mn hard magnetic alloys as promising materials for permanent magnets (review) *Russ. J. Inorg. Chem.* **65** 2007–19
[9] Yang J, Yang W, Shao Z, Liang D, Zhao H, Xia Y and Yang Y 2018 Mn-based permanent magnets *Chin. Phys. B* **27** 117503
[10] Xiang K, Huang S and Mi J 2023 Characterisations of the Al-Mn intermetallic phases formed under pulse magnetic fields solidification *IOP Conf. Ser.: Mater. Sci. Eng.* **1274** 012004
[11] Sun Q, He J, Chen J, Chen C, Guo X, Cao F and Wang S 2022 Hardness and corrosion behavior of an Al-2Mn alloy with both microstructural and chemical gradients *npj Mater. Degrad.* **6** 64
[12] Palanisamy D, Srivastava C, Madras G and Chattopadhyay K 2017 High-temperature transformation pathways for metastable ferromagnetic binary Heusler (Al–55 at.%Mn) alloy *J. Mater. Sci.* **52** 4109–19
[13] Feng H-Q, Yang Z-B, Bai Y-T, Zhang L and Liu Y-L 2020 Study on the microstructures of Al-2.5%Mn alloy *Mater. Res. Express* **7** 066527
[14] Wang Y, Xia M, Fan Z, Zhou X and Thompson G E 2010 The effect of Al_8Mn_5 intermetallic particles on grain size of As-cast Mg–Al–Zn AZ91D alloy *Intermetallics* **18** 1683–9
[15] Han G and Liu X 2016 Phase control and formation mechanism of Al–Mn(–Fe) intermetallic particles in Mg–Al-based alloys with $FeCl_3$ addition or melt superheating *Acta Mater.* **114** 54–66
[16] Sarvesha R, Ghori U-U-R, Thirunavukkarasu G, Chiu Y L, Jones I P, Jain J and Singh S S 2021 A study on the phase transformation of γ_2-Al_8Mn_5 to LT-$Al_{11}Mn_4$ during solutionizing in AZ91 alloy *J. Alloys Compd.* **873** 159836
[17] Tamura Y, Haitani T and Kono N 2006 Liquid solubility of manganese and its influence on grain size of Mg-Al Alloys *Mater. Trans.* **47** 1968–74
[18] Shechtman D, Blech I, Gratias D and Cahn J W 1984 Metallic phase with long-range orientational order and no translational symmetry *Phys. Rev. Lett.* **53** 1951–3
[19] Steurer W 2004 Twenty years of structure research on quasicrystals. Part I. Pentagonal, octagonal, decagonal and dodecagonal quasicrystals *Z. Kristallogr. Cryst. Mater.* **219** 391–446
[20] de Groot R A, Mueller F M, Engen P G and Buschow K H J 1983 New class of materials: half-metallic ferromagnets *Phys. Rev. Lett.* **50** 2024–7
[21] Özdoğan K, Aktaş B, Galanakis I and Şaşıoğlu E 2007 Influence of mixing the low-valent transition metal atoms (Y, Y^*=Cr, Mn, Fe) on the properties of the quaternary $Co_2[Y_{1-x}Y^*_x]Z$ (Z=Al, Ga, Si, Ge, or Sn) Heusler compounds *J. Appl. Phys.* **101** 073910
[22] Galanakis I, Özdoğan K, Şaşioğlu E and Blügel S 2014 Conditions for spin-gapless semiconducting behavior in Mn_2CoAl inverse Heusler compound *J. Appl. Phys.* **115** 093908
[23] Wang L Y, Dai X F, Wang X T, Cui Y T, Liu E K, Wang W H, Wu G H and Liu G D 2015 Antisite-induced half-metallicity and fully-compensated ferrimagnetism in Co–Mn–V–Al alloy *Mater. Res. Express* **2** 106101
[24] Jafari K and Ahmadian F 2017 First-principles study of magnetism and half-metallic properties for the quaternary Heusler alloys CoRhYZ (Y = Sc,Ti,Cr, and Mn;Z = Al,Si, and P) *J. Supercond. Novel Magn.* **30** 2655–64
[25] Stinshoff R, Fecher G H, Chadov S, Nayak A K, Balke B, Ouardi S, Nakamura T and Felser C 2017 Half-metallic compensated ferrimagnetism with a tunable compensation point over a wide temperature range in the Mn-Fe-V-Al Heusler system *AIP Adv.* **7** 105009
[26] Jamer M E *et al* 2017 Compensated ferrimagnetism in the zero-moment Heusler alloy Mn_3Al *Phys. Rev. Appl.* **7** 064036
[27] Umetsu R Y *et al* 2019 Half-metallicity of the ferrimagnet Mn_2VAl revealed by resonant inelastic soft x-ray scattering in a magnetic field *Phys. Rev. B* **99** 134414
[28] Han J, Wu X, Feng Y and Gao G 2019 Half-metallic fully compensated ferrimagnetism and multifunctional spin transport properties of Mn_3Al *J. Phys.: Condens. Matter* **31** 305501
[29] Khandy S A and Chai J-D 2020 Robust stability, half-metallic ferrimagnetism and thermoelectric properties of new quaternary Heusler material: a first principles approach *J. Magn. Magn. Mater.* **502** 166562
[30] Nepal S, Dhakal R and Galanakis I 2020 *Ab initio* study of the half-metallic full-Heusler compounds Co_2ZAl [Z = Sc,Ti,V,Cr,Mn,Fe]; The role of electronic correlations *Mater. Today Commun.* **25** 101498
[31] Islam A, Zulfiqar M, Nazir S and Ni J 2021 Strain-modulated electronic and magnetic properties of Co_2TMAl *Mater. Today Commun.* **26** 101764
[32] Wang G *et al* 2022 Suppression of Co-Cr antisite defect and robust half metallicity in CoMCrAl (M = Mn, Fe) Heusler Alloys *J. Alloys Compd.* **891** 161856
[33] Gupta S, Chakraborty S, Pakhira S, Barreteau C, Crivello J-C, Bandyopadhyay B, Greneche J M, Alleno E and Mazumdar C 2022 Coexisting structural disorder and robust spin-polarization in half-metallic FeMnVAl *Phys. Rev. B* **106** 115148
[34] Kumar A, Chaudhary S and Chandra S 2024 Effect of point defects and lattice distortions on the structural, electronic, and magnetic properties Co_2MnAl Heusler alloy *Phys. Rev. Mater.* **8** 034405
[35] Li J, Chen H, Li Y, Xiao Y and Li Z 2009 A theoretical design of half-metallic compounds by a long range of doping Mn for Heusler-type Cr_3Al *J. Appl. Phys.* **105** 083717

[36] Bland J A 1958 Studies of aluminum-rich alloys with the transition metals manganese and tungsten. II. The crystal structure of δ(Mn-Al)-Mn_4Al_{11} *Acta Crystallogr.* **11** 236–44
[37] Kontio A, Stevens E D, Coppens P, Brown R D, Dwight A E and Williams J M 1980 New investigation of the structure of Mn_4Al_{11} *Acta Crystallogr. B* **36** 435–6
[38] Godecke T and Koster W 1971 Eine erganzung zum aufbau des system aluminium-mangan (A supplement to the constitution of the aluminum-manganese system) *Z. Metallkd.* **62** 727–32
[39] Dunlop J B and Grüner G 1976 One-dimensional effects in the intermetallic compound $Al_{11}Mn_4$ *Solid State Commun.* **18** 827–9
[40] Niemann S and Jeitschko W 1993 The crystal structures of Re_2Al, Re_4Al_{11}, and $ReAl_6$ *Z. Naturforsch. B* **48** 1767–73
[41] Grushko B, Przepiórzyński B, Kowalska-Strzęciwilk E and Surowiec M 2006 New phase in the high-Al region of Al-Cr *J. Alloys Compd.* **420** L1–4
[42] Grushko B, Kowalski W, Pavlyuchkov D, Balanetskyy S and Surowiec M 2009 On the constitution of the Al-rich part of the Al–Cr–Mn system *J. Alloys Compd.* **468** 87–95
[43] Rigaku Oxford Diffraction CrysAlisPro 2022 version 171.42.49 (Rigaku Corporation, Oxford, UK)
[44] Betteridge P W, Carruthers J R, Cooper R I, Prout K and Watkin D J 2003 CRYSTALS version 12: software for guided crystal structure analysis *J. Appl. Crystallogr.* **36** 1487
[45] Palatinus L and Chapuis G 2007 SUPERFLIP—A computer program for the solution of crystal structures by charge flipping in arbitrary dimensions *J. Appl. Crystallogr.* **40** 786–90
[46] Groom C R, Bruno I J, Lightfoot M P and Ward S C 2016 The Cambridge structural database *Acta Crystallogr. B* **72** 171–9
[47] Dal Corso A 2014 Pseudopotentials periodic table: from H to Pu *Comput. Mater. Sci.* **95** 337–50
[48] Bergerhoff G and Brown I D 1987 Inorganic crystal structure database *Crystallographic Databases* (International Union of Crystallography) pp 77
[49] Wu H, Zhang M, Xu B and Ling G 2014 Preparation and characterization of $Al_{11}Cr_4$ phase by diffusion of Al/Cr composite film *J. Alloys Compd.* **610** 492–7
[50] Raghavan V 2009 Al-Cr-Mn (Aluminum-Chromium-Manganese) *J. Phase Equilib. Diffus.* **30** 620–3
[51] Mugiraneza S and Hallas A M 2022 Tutorial: a beginner's guide to interpreting magnetic susceptibility data with the Curie-Weiss law *Commun. Phys.* **5** 95
[52] Néel M L 1948 Propriétés magnétiques des ferrites; ferrimagnétisme et antiferromagnétisme *Ann. Phys.* **12** 137–98
[53] Smart J S 1955 The Néel theory of ferrimagnetism *Am. J. Phys.* **23** 356–70
[54] Morrish A H 1965 *The Physical Principles of Magnetism* (Wiley)
[55] Néel L 1971 Magnetism and local molecular field *Science* **174** 985–92
[56] Semboshi S, Umetsu R Y, Kawahito Y and Akai H 2022 A new type of half-metallic fully compensated ferrimagnet *Sci. Rep.* **12** 10687
[57] Stinshoff R, Nayak A K, Fecher G H, Balke B, Ouardi S, Skourski Y, Nakamura T and Felser C 2017 Completely compensated ferrimagnetism and sublattice spin crossing in the half-metallic Heusler compound $Mn_{1.5}FeV_{0.5}Al$ *Phys. Rev. B* **95** 060410
[58] Lee C-H, Chin H-H, Zeng K-Y, Chang Y-J, Yeh A-C, Yeh J-W, Lin S-J, Wang C-C, Glatzel U and Huang E-W 2022 Tailoring ferrimagnetic transition temperatures, coercivity fields, and saturation magnetization by modulating Mn concentration in $(CoCrFeNi)_{1-x}Mn_x$ high-entropy alloys *Front. Mater.* **9** 824285
[59] Webb D J, Marshall A F, Sun Z, Geballe T H and White R M 1988 Coercivity of a macroscopic ferrimagnet near a compensation point *IEEE Trans. Magn.* **24** 588–92
[60] Furukawa N 2000 Unconventional one-magnon scattering resistivity in half-metals *J. Phys. Soc. Japan* **69** 1954–7